

**Elastic neutron scattering at 96 MeV from  $^{12}\text{C}$  and  $^{208}\text{Pb}$** 

J. Klug,<sup>1</sup> J. Blomgren,<sup>1,\*</sup> A. Ataç,<sup>1</sup> B. Bergenwall,<sup>1</sup> A. Hildebrand,<sup>1</sup> C. Johansson,<sup>1</sup> P. Mermod,<sup>1</sup> L. Nilsson,<sup>1,3</sup> S. Pomp,<sup>1</sup> U. Tippawan,<sup>1</sup> K. Elmgren,<sup>2</sup> N. Olsson,<sup>2</sup> O. Jonsson,<sup>3</sup> A. V. Prokofiev,<sup>3</sup> P.-U. Renberg,<sup>3</sup> P. Nadel-Turonski,<sup>4</sup> S. Dangtip,<sup>5</sup> P. Phansuke,<sup>5</sup> M. Österlund,<sup>6</sup> C. Le Brun,<sup>7</sup> J. F. Lecolley,<sup>7</sup> F. R. Lecolley,<sup>7</sup> M. Louvel,<sup>7</sup> N. Marie-Noury,<sup>7</sup> C. Schweitzer,<sup>7</sup> Ph. Eudes,<sup>8</sup> F. Haddad,<sup>8</sup> C. Lebrun,<sup>8</sup> A. J. Koning,<sup>9</sup> and X. Ledoux<sup>10</sup>

<sup>1</sup>*Department of Neutron Research, Uppsala University, Box 525, S-75120 Uppsala, Sweden*

<sup>2</sup>*Swedish Defence Research Agency (FOI), Stockholm, Sweden*

<sup>3</sup>*The Svedberg Laboratory, Uppsala University, Uppsala, Sweden*

<sup>4</sup>*Department of Radiation Sciences, Uppsala University, Uppsala, Sweden*

<sup>5</sup>*Department of Physics, Chiang Mai University, Chiang Mai, Thailand*

<sup>6</sup>*Department of Physics, University of Jönköping, Jönköping, Sweden*

<sup>7</sup>*LPC, ISMRA et Université de Caen, CNRS/IN2P3, Caen, France*

<sup>8</sup>*SUBATECH, Université de Nantes, CNRS/IN2P3, Nantes, France*

<sup>9</sup>*NRG, Petten, The Netherlands*

<sup>10</sup>*DPTA/SPN CEA, Bruyères-le-Châtel, France*

(Received 19 June 2003; published 12 December 2003)

A facility for detection of scattered neutrons in the energy interval 50–130 MeV, SCANDAL, has recently been installed at the 20–180 MeV neutron beam line of the The Svedberg Laboratory, Uppsala. Elastic neutron scattering from  $^{12}\text{C}$  and  $^{208}\text{Pb}$  has been studied at 96 MeV in the  $10^\circ$ – $70^\circ$  interval. The achieved energy resolution, 3.7 MeV, is about an order of magnitude better than for any previous experiment above 65 MeV incident energy. The present experiment represents the highest neutron energy where the ground state has been resolved from the first excited state in neutron scattering. A novel method for normalization of the absolute scale of the cross section has been used. The estimated normalization uncertainty, 3%, is unprecedented for a neutron-induced differential cross section measurement on a nuclear target. The results are compared with modern optical model predictions based on phenomenology or microscopic nuclear theory.

DOI: 10.1103/PhysRevC.68.064605

PACS number(s): 25.40.Dn, 24.10.Ht, 28.20.Cz

**I. INTRODUCTION**

The traditional basic physics motivation for elastic (and inelastic) neutron scattering around 100 MeV is to determine the isovector term in the nucleon-nucleus interaction [1]. Coulomb repulsion of protons creates a neutron excess in all stable nuclei with  $A > 40$ . Incident protons and neutrons interact differently with this neutron excess. An isovector coupling term was introduced into the optical model by Lane [2] with the form

$$U_N(E) = U_0(E) + (4/A)U_1(E)\vec{t} \cdot \vec{T},$$

where  $\vec{t}$  is the isospin of the projectile and  $\vec{T}$  is the isospin of the target. The origin of this term may be traced to the  $\vec{\tau}_i \cdot \vec{\tau}_j$  term in the nucleon-nucleon interaction. The diagonal terms of the  $\vec{t} \cdot \vec{T}$  matrix display the differences between proton-nucleus and neutron-nucleus elastic scatterings, i.e.,

$$U_N(E) = U_0(E) \pm \epsilon U_1(E) + \Delta U_c,$$

where  $\epsilon = (N-Z)/A$  and  $\Delta U_c = 0$  for neutrons.

This expression shows that the proton-nucleus optical potential contains both an isovector term  $U_1$  and a Coulomb correction term  $\Delta U_c$  that accounts for the reduced kinetic

energy—compared to a neutron of the same incident energy—of the proton inside the nucleus. In a relativistic approach, this Coulomb correction is unambiguously linked to the central vector potential. Once  $\Delta U_c$  is known, the isovector potential  $U_1$  can be deduced by a comparison of neutron and proton elastic scattering from the same  $T \neq 0$  nucleus at the same energy.

It has been a common prejudgement in nuclear physics that the isovector term depends on  $(N-Z)/A$ , but this might be open to question. One serious problem has been observed when using the Ohio-State Dirac phenomenology for proton-nucleus scattering to calculate the neutron total cross section. Such calculations describe the  $^{16}\text{O}$  total cross section almost perfectly, while serious discrepancies for  $^{208}\text{Pb}$  provide compelling testimony for the further need to investigate the isovector nucleon-nucleus interactions.

There has been notable progress lately in theoretical studies of elastic scattering of nucleons from nuclei at intermediate energies. The early hope of nuclear physics, namely, that nuclear forces derived from the analysis of nucleon-nucleon data could be used to predict nuclear many-body phenomena, is maybe finally being realized. In recent calculations [3], the only input is the nucleon-nucleon force and the wave functions of the target nuclei. The  $NN$  potentials (below the pion production threshold) now might be good enough so that uncertainties in these calculations largely reflect the uncertainties in the nuclear densities. In particular, analyses of proton data together with accurate neutron scat-

\*Corresponding author. Email address: jan.blomgren@tsl.uu.se

tering data may at last be able to yield information regarding the relative distribution of charged and uncharged matter in nuclei.

Neutron elastic scattering at small angles is of special interest because the Coulomb bump masks the nuclear amplitude in the proton case. Larger angle data are important to test the limits of the first-order theory and to pin down the diffraction structure with increased confidence. In future, neutron spin observables would be most welcome to complement the extensive proton measurements.

The targets for a survey of neutron elastic scattering would primarily be the closed-shell nuclei experimentally available. In the present paper, neutron elastic scattering data on  $^{12}\text{C}$  and  $^{208}\text{Pb}$  at 96 MeV are presented. They constitute the first two nuclei in a series of experiments, while data on  $^1\text{H}$ ,  $^2\text{H}$ ,  $^{16}\text{O}$ ,  $^{56}\text{Fe}$ , and  $^{89}\text{Y}$  are under analysis.

Several different fields of basic nuclear physics would benefit from better knowledge of the optical potentials. The lack of precise neutron optical potentials is a serious constraint for both  $(p, n)$  and  $(n, p)$  studies in this energy domain. A 20%–30% uncertainty has been ascribed in the calculation of absolute  $(p, n)$  cross sections to uncertainties in the optical potentials [4]. Other fields where such potential information would be of large interest are  $(e, e'pn)$ ,  $(\gamma, n)$ , and  $(p, pn)$  experiments.

The interest in high-energy neutron data is rapidly growing, since a number of potential large-scale applications involving fast neutrons are under development, or have been identified. These applications primarily fall into three sectors; nuclear energy and waste, nuclear medicine, and effects on electronics.

The recent development of high-intensity proton accelerators has resulted in ideas to use subcritical reactors, fed by neutrons produced in spallation processes maintained by external proton beams, for transmutation of waste from nuclear power reactors or nuclear weapons material. This might result in less problematic waste material and/or energy production. New nuclear data are needed for feasibility assessments of these techniques. The present work is part of the EU project HINDAS (high and intermediate energy nuclear data for accelerator-driven systems), which has been designed to meet this demand [5].

Conventional radiation treatment of tumors, i.e., by photons or electrons, is a cornerstone in modern cancer therapy. Some rather common types of tumors, however, cannot be treated successfully. For some of these, very good treatment results have been obtained with neutron therapy [6].

During the last few years, it has become evident that electronics in airplanes suffer effects from cosmic-ray neutrons [7,8]. For instance, a neutron can induce a nuclear reaction in the silicon substrate of a memory device, releasing free charge, which flips one or more memory units. Similar effects causing soft- and/or hardware damage have recently been identified also at ground level.

Finally, neutrons at commercial aircraft altitudes induce significant radiation doses to the airplane personnel [9].

For all these applications, an improved understanding of neutron interactions are needed for calculations of neutron transport and radiation effects. It should be emphasized that

what is primarily needed is not raw data, because for these applications, it is beyond reasonable efforts to provide complete datasets. Instead, the nuclear data needed for a better understanding must come to a very large degree from nuclear scattering and reaction model calculations, which all depend heavily on the optical model, which in turn is determined by elastic scattering and total cross section data.

Very little high-quality neutron data exist above 20 MeV energy (which is the upper energy limit of the established evaluated data libraries for fission and fusion applications). There are high-quality neutron total cross section data on a series of nuclei up to about 600 MeV [10]. In addition,  $(n, p)$  data in the forward angular range at modest excitation energies are available up to about 300 MeV for a rather large number of nuclei [11,12].

The  $np$  scattering cross section has been measured extensively [13]. On the other hand, for neutron elastic scattering from nuclei heavier than the light ions (i.e., for  $A \geq 6$ ), there are very few measurements. Above 30 MeV neutron energy, only two experiments have produced data with an energy resolution adequate for resolving individual nuclear states, an experiment from MSU at 30 and 40 MeV [14,15], and from UC Davis at 65 MeV [16,17]. Recently, experiments at 55, 65, and 75 MeV were reported, having energy resolutions in the 10–20 MeV range [18,19]. In addition, a few measurements in the  $0^\circ$ – $30^\circ$  range, between 80 and 350 MeV, are available; all with energy resolutions of 15 MeV or more [20–24]. This poor resolution is, however, not a significant drawback at such small angles because elastic scattering dominates heavily, but at larger angles such a resolution would make data very difficult to interpret. An overview of the neutron elastic scattering experiments is given in Table I, where measured nuclei, neutron energies, energy resolutions, and angular ranges are shown.

A brief account of the results presented in this paper has been published recently [25], and in the present paper, the analysis and the results are discussed in some detail.

## II. EXPERIMENTAL ARRANGEMENT

### A. Neutron beam and detector setup

The neutron beam facility at the The Svedberg Laboratory, Uppsala, Sweden, has recently been described in detail [26], and therefore only a brief description is given here. An overview is presented in Fig. 1. Protons from the cyclotron impinge on a  $427 \text{ mg/cm}^2$  disc of isotopically enriched (99.98%)  $^7\text{Li}$  from the left, producing  $96 \pm 0.5 \text{ MeV}$  [ $1.2 \text{ MeV FWHM}$  (full width at half maximum)] neutrons by the  $^7\text{Li}(p, n)$  reaction. The low-energy tail of the source neutron spectrum was suppressed by time-of-flight techniques. After the target, the proton beam is bent into a well-shielded beam dump. A system of three collimators defined a 9-cm-diameter neutron beam at the scattering target, where the neutron yield was typically  $6 \times 10^5 \text{ s}^{-1}$  over the whole beam area. The neutron beam was dumped in a tunnel about 10-m downstream of the experimental position.

Scattered neutrons were detected by the SCANDAL (SCattered Nucleon Detection AssembLy) setup (see Fig. 2), where the neutron energy is determined by measuring the

TABLE I. Neutron elastic scattering experiments with neutron energies  $E_n \geq 30$  MeV.

Reference	Target	Energy (MeV)	Resolution (MeV at FWHM)	Angular range (deg)
[14,15]	Ca, Si	30, 40	0.15	15–140
[18,19]	C, Si, Fe, Zr, Pb	55, 65, 75	10–20	2–57
[17]	C, Si, Ca, Fe, Sn, Pb	65	2.7	6–50
[20]	Al, Cu, Pb	84	30	2–25
[21]	Li, Be, C, Al, Cu, Cd, Pb, U	96	24	1–29
[22]	Li, Be, C, N, O, Al, Cu, Cd, Pb	136	27	0–20
[23]	C, Al, Cu, Cd, Pb	155	60	3–30
[24]	C, Al, Cu, Sn, Pb	350	15	1–20
Present experiment	C, Pb	96	3.7	10–70

energy of proton recoils from a plastic scintillator, and the neutron scattering angle is determined by tracking the recoil proton. For a comprehensive description of its technical details, and of the experimental procedure, see Ref. [26]. It is primarily intended for studies of elastic neutron scattering, but can be used for  $(n, p)$  and  $(n, d)$  reaction experiments as well. Direct proton detection is also utilized at the beginning of every experiment in order to calibrate the detectors.

The setup consists of two identical systems, in their standard positions placed to cover  $10^\circ$ – $50^\circ$  and  $30^\circ$ – $70^\circ$ , respectively. In the present experiment, each arm consisted of a 2-mm-thick veto scintillator for fast charged-particle rejection, a 10-mm-thick neutron-proton converter scintillator, a 2-mm-thick plastic scintillator for triggering, two drift chambers for proton tracking, a 2-mm-thick  $\Delta E$  plastic scintillator which was also part of the trigger, and an array of CsI detectors (12 on each arm) for energy determination of recoil protons produced in the converter by  $np$  scattering. While the CsI detectors have one photomultiplier (PM) tube each, the plastic scintillators have two, mounted adjacent to each other on one of the longer horizontal sides. This design has been chosen in order to allow the spectrometer arms to be placed close to the beam.

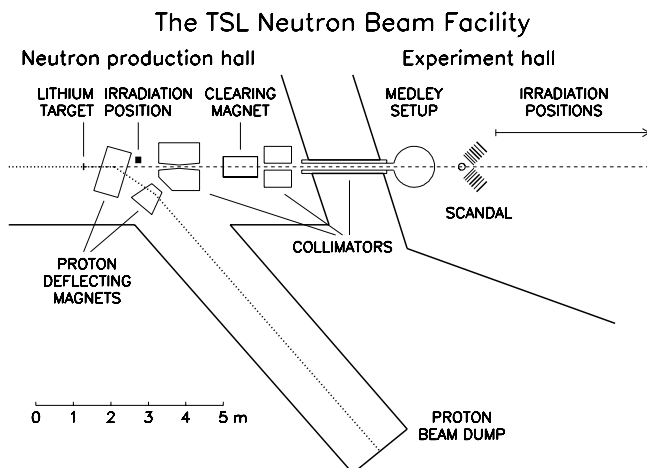


FIG. 1. Overview of the Uppsala neutron beam facility.

The trigger, when detecting neutrons, was provided by a coincidence of the two trigger scintillators, with the front scintillator acting as a veto. The total neutron energy resolution varies with individual CsI crystals, but is on average 3.7 MeV (FWHM).

## B. Experimental procedure

The experiment was carried out in two different runs of about one week each. At the beginning of each campaign, a  $\text{CH}_2$  target was placed in the neutron beam for calibration purposes, by detecting recoil protons from  $np$  scattering. At one of the occasions, a multitarget arrangement was used to increase the target content without impairing the energy resolution. This multitarget box allows up to seven targets to be mounted simultaneously, interspaced with multiwire proportional counters (MWPC). In this way it is possible to determine in which target the reaction took place, and corrections for energy loss in the subsequent targets can be applied. Two additional MWPCs, upstream of the targets, act as veto detectors for charged particles accompanying the neutron beam. A more detailed description is given in Ref. [27].

At the other occasion, the multitarget was unavailable, and a single  $\text{CH}_2$  sheet, 1 mm thick, served as the calibration target. Direct detection of recoil protons with well-defined

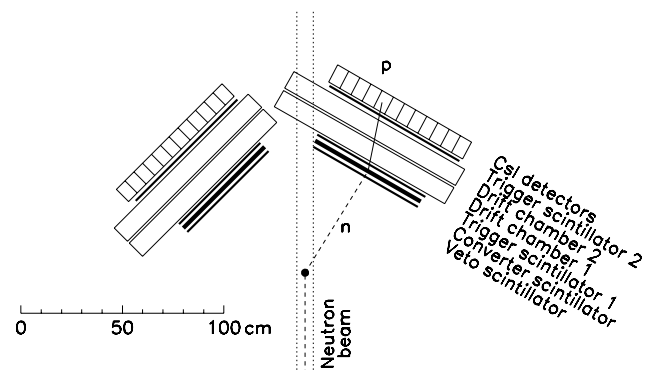


FIG. 2. Schematic layout of the SCANDAL setup. A typical event is indicated.

energies, coming from  $np$  scattering in the calibration target, was accomplished by removing the veto signals from the trigger.

The advantages of using the multitarget in the calibration runs are shorter data taking time because a larger amount of target material can be used while retaining a good resolution, and the fact that a  $^{12}\text{C}(n,p)$  background spectrum can be recorded simultaneously (using a pure carbon target). This background can be subtracted in order to isolate the recoil protons originating from the hydrogen atoms. However, the data taking time is rather short also when using a single  $\text{CH}_2$  sheet, and the recoil protons from  $np$  scattering form a prominent peak in the histograms even before background subtraction. Moreover, the  $^{12}\text{C}(n,p)$  reaction has a  $Q$  value of  $-12.6$  MeV, which makes the  $np$  scattering peak kinematically separated from the carbon background at small angles. This means that it is not crucial to use the multitarget for calibration purposes.

In  $(n,n)$  measurements, the multitarget is normally placed empty upstream of the scattering target and used as an extremely thin charged-particle veto detector. Fortunately, it has been shown that the contamination of charged particles in the neutron beam and thereby the effect of the multitarget veto is very small. This will be elaborated upon in Sec. III.

After collecting calibration data, the setup was modified for neutron detection by utilizing the veto scintillator signals for charged-particle rejection. The lower limit of the angular range,  $10^\circ$ , represents an arm position where the scintillator detectors barely avoid being hit by the neutron beam while the upper limit,  $70^\circ$ , has been chosen since reliable statistics cannot at present be obtained in a one-week experiment at larger angles. The angular region covered by both arms,  $30^\circ$ – $50^\circ$ , facilitates estimation of the consistency of the results, and of possible systematical differences between the two arms.

Two scattering targets were used, a carbon cylinder, 5 cm high and 5 cm in diameter, with a mass of 178 g and natural isotopic composition (98.9%  $^{12}\text{C}$ ), and a radiogenic lead cylinder (88%  $^{208}\text{Pb}$ , 11%  $^{206}\text{Pb}$ , and 1%  $^{207}\text{Pb}$ ), 6.3 cm high and 2.9 cm in diameter, with a mass of 444 g. During a typical experiment week, the data taking began and ended with the  $^{208}\text{Pb}$  target in the beam, and in between,  $^{12}\text{C}$  and background (no target) data were taken.

The vacuum system in which the neutron beam is transported is terminated by a 0.1-mm-thick stainless steel foil, 80-cm upstream of the scattering target position. Immediately after the foil, a fission detector for absolute monitoring of the neutron fluence, based on thin-film breakdown counters [28], is mounted.

The vacuum termination foil and the fission detector act as neutron scatterers, giving a background of neutrons that did not scatter in the real scattering target further downstreams. Since SCANDAL is triggered by protons coming from the neutron-proton converter scintillators, it is not possible to know the history of the neutrons before their arrival to the converter. Therefore, one cannot distinguish event-by-event between neutrons coming from the scattering target and neutrons from, e.g., the fission detector. For part of the data taking time, a lead collimator was installed around the

neutron beam, between the fission detector—or, if it was used, between the multitarget box—and the scattering target position. The collimator was constructed of 10-cm-thick lead blocks, placed parallel to the neutron beam. Its effect was studied by comparing data from runs with, and without, the collimator installed. The effects of the collimator will be discussed later.

Downstream of the target position, the neutron beam goes through the drift chambers of the small-angle arm (located at the right side of the beam) of SCANDAL. This is very little material, and located such that only neutrons emitted backwards can cause triggers. Thereby, the setup itself produces very little background; in fact, the no-target data are consistent with neutron scattering in nothing but the air around the target region.

The dead time in the data acquisition system was around 4% during the experiment.

### III. DATA ANALYSIS

#### A. Calibration

The data were analyzed off line on an event-by-event basis. In a first stage, the time information from the drift chambers was converted to positions; angular information and detector hit positions of the particle trajectories were calculated, based on the obtained drift chamber coordinates; and the registered pulse heights (PH) in the CsI and plastic scintillator detectors were converted to energy, using the proton detection data from the beginning of the experiment.

During this process, about two-thirds of all events were rejected. Each event had to pass several criteria to be accepted. The main reason for discarding events at this stage of the analysis was the requirement that at least one CsI detector in the event had a PH above a certain threshold value.

For the drift chambers, it was at the same time required that the calculated coordinates of the detected particle corresponded to a position within the volume between the trigger scintillators. The coordinates were also used to trace the trajectories of the protons, which in turn were used to establish the hit positions for the CsI detectors and the conversion points in the converter scintillators. The conversion depth was obtained from the pulse height information. At the same time, the elastic neutron scattering angle in the target and the proton recoil scattering angle, or conversion angle with respect to the direction of the neutron hitting the converter, were calculated.

Each drift chamber should in the ideal case give one horizontal and one vertical coordinate. Since only two drift chambers on each arm were used for tracking, multiple hits in the drift chambers resulted in ambiguities. In around 10% of the events, more than one wire in a drift chamber plane fired due to crosstalk within the drift chamber, an effect which was investigated already at the commissioning of these drift chambers. In such events, the wire that fired first was selected in the analysis, since signals induced by crosstalk come later in time. A separate test experiment using four drift chambers for overdetermination of proton tracks has shown that this algorithm results in a correct identification in about 90% of the cases, leaving about 1% of the

events in the present experiment with incorrect position information for one of the four position coordinates. Essentially all these incorrect events were removed using the presence of a hit in the correct CsI as a consistency check.

For the calibration of the CsI detectors, two calibration points per detector were used: a pedestal channel due to events detected in other CsI crystals, and thus associated with zero PH and energy, and an  $np$  proton peak. The centroid channel of the proton peak was found by fitting it with a Gaussian. The calibration was done by a two-step procedure. In the first step, the deposited energy represented by the centroid channel of the proton peak was obtained by calculating the energy loss of protons between the target and the CsI detector in question. In the second step, after having calibrated the plastic scintillator detectors (see below), the deposited energy represented by the proton peak was found by adding the actually measured energy losses in the scintillator detectors, to energy losses that were calculated for materials in which the protons were not detected (such as the wrapping covering the scintillators).

A linear correspondence was assumed between PH and deposited energy. This should be a reasonably good assumption for CsI in the present application [29]. However, due to detector geometry and local variations in the light output within a CsI crystal, the protons, having the same energy, give rise to different PH values along the vertical axis in the crystal. The reason for this vertical dependence is that the crystals have a rather elongated, trapezoidal shape; 30 cm high with a  $7.7 \text{ cm}^2$  cross section area at the PM tube end and a  $5.5 \text{ cm}^2$  area at the other end. If not compensated for, this geometry effect will contribute up to half the intrinsic energy resolution in the CsI detectors. Therefore, when calculating the energy deposited in the CsI crystal, the coordinate of the vertical hit position on the detector was used to select the calibration PH value that correctly corresponds to the  $np$  proton peak energy.

The plastic scintillator detectors were calibrated using events where protons hit a narrow, central section of the scintillator, i.e., where the distance is approximately the same to both PM tubes, and where it can be assumed that these detect half the light each from the energy deposited. Each PM tube was calibrated separately. By selecting  $np$  scattering events, i.e., events that appear in the peak in a CsI energy spectrum, a peak in the plastic scintillator PH spectrum was identified. The energy represented by the centroid of that peak was obtained by correcting for the calculated energy losses in upstream material. The pedestal channel gave a second calibration point for each PM tube. A linear correspondence was assumed between PH and energy. Finally, the total energy  $\Delta E$  detected by a plastic scintillator was obtained as the sum of the energies from the two PM tubes.

Geometry effects also appear in the plastic scintillators. Protons that deposit the same energy at different locations in the detectors give different  $\Delta E$  values in the calculation described above. By mapping the deviation of the measured  $\Delta E$  value from the expected one, as a function of the proton hit position on the scintillator in both vertical and horizontal coordinates, it was concluded that the location of the PM

tubes, adjacent to each other on the same side of the scintillator, was the main reason for this effect. It was also found that the effect is significant only in the converter scintillators, which can be explained by their relative thickness (compared with the trigger detectors). A compensation for this geometry dependence was done when calculating  $\Delta E$  in the converter detectors, by including a position-dependent term describing the mapped-out deviation.

The energy loss in materials where the protons are not detected, such as detector wrapping, drift chamber foils, and air, was calculated based on the energies detected in the trigger scintillators and in the CsI detector.

The total energy of the charged particle, emitted in the calibration target in the case of proton detection or in the converter, as in the case of elastic neutron scattering, was obtained as the sum of the detected energy losses and the estimated energy loss in other materials. Finally, for the elastic scattering events, the neutron energy at the conversion to a proton, and the excitation energy, were calculated using the scattering angle, the conversion angle, and the total energy. This gave excitation-energy spectra for 24 different angles in the laboratory system, related to the position of the CsI crystal in which the proton was stopped.

## B. Data reduction

In a second stage of the analysis, gates on the positions, angles, and energies that had now been associated with the accepted events were applied to extract the contents in the ground state peaks, representing elastic scattering, from the excitation-energy spectra. This was done for  $^{208}\text{Pb}$  and  $^{12}\text{C}$  data, as well as for background data. Each CsI detector defined an angular bin, and events belonging to a specific bin were selected by setting a gate on the detected CsI energy.

A  $\Delta E-E$  technique was used to separate protons from other charged particles, mostly deuterons, originating from the converter. Gates in the form of two-dimensional contours were applied to scatter plots if the sum of the detected energy losses in the two trigger scintillators was plotted against the energies in the CsI detectors. The separation between protons and deuterons was good enough to make the assignment of particle identity a straightforward procedure. This cut was, however, not of crucial importance in the extraction of elastic scattering events, since the  $Q$  value for  $^{12}\text{C}(n, d)$  is  $-13.7 \text{ MeV}$ , i.e., there is no physical background of deuterons in the energy range of elastic scattering.

The energy determination for events where a proton passes through more than one CsI detector is very poor, due to large straggling effects in CsI wrapping material. Therefore, plots were made of vertical versus horizontal hit positions on the CsI crystals. In these scatter plots, two-dimensional gates were applied to select events where a minimum distance to the edges assured that the protons were stopped in a single detector. As this gate also identified the CsI detector being hit, it was required that it should be consistent with the selection done with the energy gate or else the event was discarded.

A gate on the neutron time of flight (TOF) was used to suppress the number of events coming from the low-energy

tail in the neutron beam spectrum. The TOF was defined by the time difference between trigger 1 and a signal generated by the cyclotron rf, and the information was corrected for the flight time from the scattering target to trigger 1. In the present experiment, this information is, however, not important. The reason is that a low-energy neutron in the beam cannot induce emission of a full-energy neutron from the scattering target. The TOF cut left the number of events in the ground state peaks unchanged, thereby verifying that there is no background that simulates elastic scattering. For planned future experiments on inelastic scattering, the TOF information is, however, of crucial importance.

Besides hydrogen, the scintillator detectors contain carbon, and the  $Q$  value for  $^{12}\text{C}(n,p)$  is  $-12.6$  MeV. Thus, at forward conversion angles, energy detection alone can isolate the protons which are due to conversion of elastically scattered neutrons in hydrogen. At about  $20^\circ$  conversion angle, however, the proton energies from the two processes are the same, and thereby it can no longer be determined whether the energy lost is due to excitations in the neutron scattering sample or in the conversion. By applying a maximum converter scattering angle criterion, such problems can be avoided. The energy resolution in SCANDAL requires an upper limit of the converter scattering angle in the  $10^\circ$ – $15^\circ$  range for a good separation. By comparing excitation-energy spectra obtained with different values of the maximum converter scattering angle it is concluded that  $10^\circ$  is suitable since a small angle facilitates the separation of the ground state peak, even if it is at the expense of statistics.

For some of the recorded events, the conversion had taken place in the first trigger scintillator instead of the converter. These events formed a peak at zero energy in the  $\Delta E$  spectrum of the converter, and could thus easily be removed.

When analyzing data from the experiment where the multitarget was used, events contaminated with charged particles in the neutron beam were rejected by requiring that no MWPC in the multitarget had fired.

The multitarget data were also used to estimate the relative number of charged particles in the beam. The first chamber detected particles from upstream of the multitarget, predominantly coming from the vacuum termination foil and the fission detector, as well as charged particles due to conversions within the multitarget, up to the position of the first chamber. The second chamber detected the same particles, plus particles created between the first and the second chamber. This information could be used to extract the number of particles created in each multitarget plane, which in turn was used in the determination of the number of charged particles coming from upstream of the multitarget. A comparison with the total number of accepted events (surviving all gates) showed that the fraction of charged particles in the neutron beam was less than 1%.

In the experiment where the multitarget was not used as a veto detector, this fraction could not be removed in a direct way. However, charged particles that scattered into the SCANDAL arms were removed by the veto detectors. Only if they caused  $(p,n)$  reactions in the scattering target they would contribute to the data, but since the  $(p,n)$  reaction cross sections are several orders of magnitude smaller than

the elastic neutron scattering cross sections, it was concluded that the charged-particle contribution could be ignored.

The data reduction was so far done on an event-by-event basis, resulting in—for each of the two experiment weeks—excitation-energy spectra at 24 angles, in the range  $10^\circ$ – $70^\circ$  in the laboratory system. The spectra were of three types, depending on the scattering target: elastic scattering from  $^{208}\text{Pb}$  including background, elastic scattering from  $^{12}\text{C}$  including background, and pure background data. Inspections of data from the beginning and the end of an experiment week showed that there was no drift in the system over an entire campaign. However, data from the two weeks were still analyzed separately.

In the data reduction of the signal spectra, i.e.,  $^{208}\text{Pb}$  and  $^{12}\text{C}$ , the target mass is used when defining the excitation energy. Thereby, the background in each spectrum is affected by the assumed target mass. As a consequence, the background data were sorted twice, resulting in separate background datasets for  $^{208}\text{Pb}$  and  $^{12}\text{C}$ .

For the further analysis, the excitation-energy spectra were stored as histograms. Examples are shown in Fig. 3, where the  $^{208}\text{Pb}$  and  $^{12}\text{C}$  histograms have been scaled to the neutron fluence of the background histograms, making each histogram equivalent to 17 h of data taking time. Data obtained with detectors at three different angles in the laboratory system illustrate the difference in count rate. All spectra of the same angle have similar shapes but different magnitudes. The spectra at the smallest angle clearly reflect the characteristics of the semimonoenergetic neutron beam spectrum, with a peak and a low-energy distribution, and also that elastic scattering dominates at small angles. At larger angles, the relative number of inelastic scattering events increases. The differences in magnitude at the same angle are consistent with the different amounts of target material in which the elastic scattering takes place (i.e.,  $^{208}\text{Pb}$ ,  $^{12}\text{C}$ , and air).

The background histograms were subtracted from the  $^{208}\text{Pb}$  and  $^{12}\text{C}$  excitation-energy histograms after dead time correction and normalization to the same neutron fluence, as given by the fission detector. In parallel with the treatment of the data spectra, the corresponding operations were performed on histograms containing the binwise variance for  $^{208}\text{Pb}$  and  $^{12}\text{C}$ , to be used later for estimation of the statistical errors.

### C. Extraction of elastic scattering events

The number of elastic scattering events at each angle was obtained by integrating the ground state peaks in the excitation-energy histograms in a region of  $\pm\Gamma$  around the peak centroid, where  $\Gamma$  is the FWHM. The centroid of the ground state peak and the resolution  $\Gamma$  were obtained from a Gaussian fit to the peak. This gaussian was at the same time one component in a spectrum function that was constructed in order to describe the entire spectrum up to about 15 MeV above the ground state peak. A good description of the spectrum in this interval was a condition for defining the integration limits using the resolution  $\Gamma$ . The spectrum function was established in the following way. In the  $^{12}\text{C}$  histograms, Gaussians were fitted to the ground state and to the excited

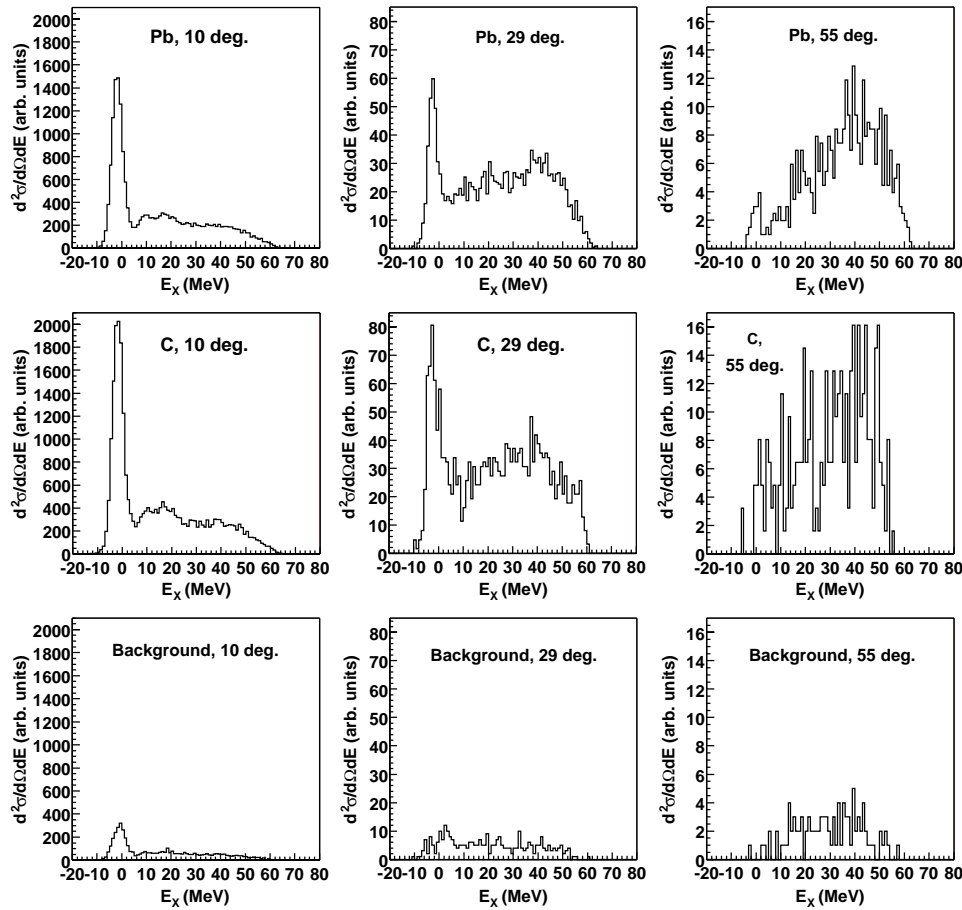


FIG. 3. Examples of  $^{208}\text{Pb}(n,n)$  and  $^{12}\text{C}(n,n)$  excitation-energy histograms before background subtraction, and pure background histograms at three different laboratory angles. The  $^{208}\text{Pb}$  and  $^{12}\text{C}$  histograms have been scaled to the neutron fluence of the background histograms.

states at 4.4 MeV ( $J^\pi=2^+$ ) and 9.6 MeV ( $3^-$ ). At an excitation energy of about 10 MeV and up, protons from  $^{12}\text{C}(n,p)$  reactions in the converter formed a rather structureless flat distribution. In a recent measurement of the  $^{12}\text{C}(n,p)^{12}\text{B}$  reaction at the present energy [72], conducted with a better energy resolution, it has been shown that excitation of the  $^{12}\text{B}$  ground state dominates the low-energy end of the excitation-energy spectrum. As a consequence, the slope of the  $^{12}\text{C}(n,p)$  distribution in the present experiment should be determined by the experimental energy resolution. Therefore, a Gaussian was fitted to account for the opening of this distribution, with a centroid at 12.6 MeV above the ground state centroid, and with the same width as for the elastic neutron scattering ground state. The spectrum function was defined as the sum of these four Gaussians. Examples at two different laboratory angles are given in Fig. 4.

The height, position, and width of the ground state Gaussian were treated as free parameters in the fit, and the same width was used for the other three Gaussians. The centroids of these were fixed relative to the ground state by the known excitation energies, i.e., 4.4, 9.6, and 12.6 MeV. The height of the Gaussian at 4.4 MeV was coupled to the height of the ground state Gaussian by a multiplicative factor, being the cross section ratio between the excited state and the ground

state at the angle in question. For this purpose, both microscopic and phenomenological calculations of the respective cross sections had been done (see below). The heights of the Gaussians at 9.6 and 12.6 MeV were, on the other hand, free parameters since it was found that this improved the overall fit.

Spectrum functions for the  $^{208}\text{Pb}$  histograms were established in an equivalent manner. In this case, the collective  $3^-$  and  $2^+$  states at 2.6 MeV and 4.1 MeV, respectively, were fitted with Gaussians (see Fig. 4). In addition to another Gaussian peak at 12.6 MeV, to account for  $^{12}\text{C}(n,p)$  reactions in the converter as described above, a fifth Gaussian was added at  $E_x=8.3$  MeV to account for a large number of weaker states between 4.1 and 12.6 MeV. The width of this Gaussian was allowed to vary with respect to the other ones. As in the case of the 4.4-MeV Gaussian in the  $^{12}\text{C}$  histograms, the heights of the 2.6- and 4.1-MeV Gaussians were linked to the height of the ground state Gaussian in  $^{208}\text{Pb}$ . Here, instead, the heights of the 8.3- and 12.6-MeV Gaussians were free.

Finally, the number of measured elastic scattering events was obtained by integrating the excitation-energy histogram in the interval  $\pm\Gamma$  around the peak centroid and correcting the result for the small contributions from the low-lying excited states.

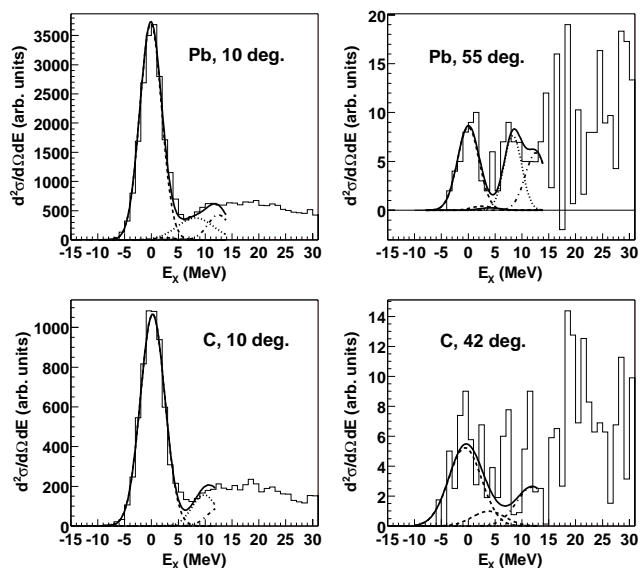


FIG. 4. Examples of spectrum functions used to extract the number of elastic scattering events from  $^{208}\text{Pb}$  and  $^{12}\text{C}$  data obtained at different laboratory angles. Upper panels:  $^{208}\text{Pb}$ . Gaussians fitted to the ground state and the  $3^-$  excited state at 2.6 MeV are dashed, the Gaussian fitted to the  $2^+$  state at 4.1 MeV (having a height close to zero) is represented by a solid line, and the Gaussian at 8.3 MeV, accounting for a large number of weaker states above 4.1 MeV, is dotted. The dash-dotted curve describes the beginning of the distribution of protons from  $^{12}\text{C}(n,p)$  reactions in the converter. The sum of these contributions form the spectrum function drawn as a solid line. Lower panels:  $^{12}\text{C}$ . Gaussians fitted to the ground state and the  $2^+$  excited state at 4.4 MeV are dashed while the Gaussian fitted to the  $3^-$  state at 9.6 MeV is dotted. The beginning of the  $^{12}\text{C}(n,p)$  proton distribution is dash dotted. See the text for details.

The variance of the number of elastic scattering events was obtained by integrating the variance histograms in the same interval as the excitation-energy histograms and applying the same types of corrections.

At large angles, the fitting procedure described above could not be used in order to extract the numbers of elastic scattering events, since there was too poor statistics in the excitation-energy histograms. Instead, the integration limits were chosen by eye. The integrated numbers were then corrected for scattering to the low-lying excited states.

Calculations of the excitation of low-lying states for the corrections above were made both phenomenologically and microscopically. Phenomenological calculations of the cross sections for scattering from the ground state and the  $3^-$  and  $2^+$  states in  $^{208}\text{Pb}$  were made using the global potential of Koning and Delaroche [30]. The same spherical optical model was employed for the ground state and the excited states, and a distorted wave Born approximation (DWBA) for the inelastic scattering from the first excited collective states was performed. From the phenomenological calculations, the cross section ratios at various angles linking the heights of the Gaussians at 2.6 and 4.1 MeV to the ground state Gaussians were obtained.

Microscopic calculations of the cross sections for scattering from the ground state and from the  $2^+$  state in  $^{12}\text{C}$  were made by van der Werf [31]. These were performed with DWBA98 [32], using the Cohen-Kurath wave function [33] calculated with OXBASH [34], with the interaction taken from von Geramb's density-dependent Paris potential for 100 MeV incident energy [35]. Distorted waves were generated from Nadasen's optical model potential for 96 MeV [36]. From these calculations, the cross section ratios at various angles linking the heights of the Gaussians at 4.4 MeV to the ground state Gaussians were obtained.

Since  $^{12}\text{C}$  is an isospin-zero nucleus, the  $(p,p)$  and  $(n,n)$  cross sections at the same energy can be expected to be very similar. Thus, these model calculations of the excitation of the  $2^+$  state can be checked using  $(p,p')$  data. It turns out that data at 96 MeV [37,57] and at 100 MeV [38] agree with the model calculation above in the angular range where the  $2^+$  excitation is significantly large to affect the ground state cross section extraction. At smaller angles, however, the model calculation overshoots the data, but in those cases the ground state is more than two orders of magnitude larger than the  $2^+$  state.

Phenomenological calculations were also done for  $^{12}\text{C}$ , but only for comparison with the microscopic calculations. The results were similar for the ground state and the  $2^+$  state in  $^{12}\text{C}$  at angles up to about  $55^\circ$ , but at larger angles the microscopic calculations gave significantly larger cross sections for excitation of the  $2^+$  state.

The solid angle for protons detected in the CsI crystals is different from detector to detector. At the same time, the number of protons in the converter seen by a neutron coming from the scattering target depends on the elastic neutron scattering angle, while the  $np$  cross section varies with conversion angle. These effects mean that the effective solid angle for detecting protons is an individual number for each CsI detector, constituted by all possible neutron and proton combinations allowed by the maximum converter scattering angle criterion and by the gate on the CsI crystal hit position. Therefore, a computer code for calculating the effective solid angle for proton detection in each CsI detector has been developed.

The converter scintillator and the stack of CsI crystals of a SCANDAL arm were divided horizontally and vertically into a number of pixels. For each converter pixel being hit by a neutron, all proton trajectories hitting the pixels of a CsI detector were examined. If the proton trajectory was accepted by the conversion angle and CsI detector hit position criteria, then the conversion efficiency for that combination of converter and CsI pixel was calculated. The conversion efficiencies for all the accepted proton trajectories between the converter pixel and the CsI detector in question were summed. The effective solid angle for detecting a proton converted in this pixel was obtained as the solid angle of the converter pixel multiplied with the summed conversion efficiency. Finally, the total, effective solid angle for detection of elastic neutron scattering events with a certain CsI detector was obtained by adding the contributions from all converter pixels, giving typically  $2 \mu\text{sr}$  per CsI detector. These pixels formed a well-defined area on the converter scintillator in

which the accepted protons were created, and this area was used to calculate the average elastic neutron scattering angle associated with that CsI detector, and the angular range covered by each CsI detector (see Sec. III E).

In addition to the effective solid angle, the proton detection efficiency has contributions from the efficiencies of each drift chamber plane (four per SCANDAL arm), the efficiency of selecting the correct wire when there are double-hit events in the drift chambers, and the CsI response. The contributions are measured to be  $0.75 \pm 0.10$  (from an average of 0.93 per plane),  $0.93 \pm 0.02$ , and  $0.92 \pm 0.01$ , respectively. This makes a total proton detection efficiency of  $0.64 \pm 0.10$ .

Since the energy resolution is different for different CsI detectors, the low-energy continuum originating from the  ${}^7\text{Li}(p, n)$  reaction will give different contributions to the full-energy  $np$  peaks at different angles (and thus to the ground state peaks in the excitation-energy spectra). This contribution, as a function of the peak width [39], has been determined using experimental neutron spectra for the  ${}^7\text{Li}(p, n)$  reaction measured by Byrd and Sailor [40]. Correction factors resulting from this relationship were used when calculating the cross sections. Because this effect is small (around 4%), its influence on the correction for scattering to excited states, also being small, was not taken into account.

#### D. Cross section calculation and normalization

Angular distributions for elastic neutron scattering cross sections were extracted separately for the two experiment weeks (for both  ${}^{208}\text{Pb}$  and  ${}^{12}\text{C}$ ), and then merged to a single distribution per nucleus by means of weighted averages. Thereafter, the distributions were corrected for neutron attenuation and multiple scattering in the target, using a MONTE CARLO program [41].

In an extended target, part of the neutron flux will be lost from the elastic channel by other reactions, resulting in a reduced count rate, but this does not affect the angular resolution of the experimental cross section. Therefore, this can be expressed as a single attenuation correction factor. Neutrons having been scattered elastically more than once give a smearing effect on the experimental cross section. Such an effect arises also from the angular spread in single scattering: due to the size of the target, the scattering angle can be slightly different from the angle between the direction of the incoming neutron and the direction from the center of the target to the detector. Finally, if the cross section varies rapidly, the average scattering angle does not necessarily correspond to scattering from the target center.

The input to the MONTE CARLO code was an angular distribution given in the laboratory system. After conversion to the center of mass (c.m.) system and calculation of the attenuation, the code simulated the experiment. The output was an angular distribution that was slightly smoothed with respect to the structure of maxima and minima of the input. For the measured SCANDAL data, the point was to find a distribution that, when used as input to the simulation, resulted in an output reproducing the measured angular distribution. The input was then considered as the “true” angular distribution, i.e., unaffected by multiple scattering. In prac-

tice, this was done by using the measured angular distribution as the input to the simulation. The smoothed distribution obtained as the output was then “mirrored” in the original one, producing a distribution with a more pronounced structure. The simulation was then repeated with this new distribution as the input. If the output from the second simulation agreed relatively well with the original, experimental distribution, then the input to this simulation was taken to be the final, corrected result with respect to multiple scattering and target geometry. If not, the procedure of mirroring and simulation was iterated until the desired agreement was reached.

The mirroring was done in a Legendre polynomial fit to the experimental distribution, since a direct mirroring in the measured points would have magnified deviations of individual points from a smooth curve in the process. In order to get a successful Legendre polynomial description of the measured angular distribution, the data have to reproduce the structure of maxima and minima in a satisfactory way. In the case of  ${}^{208}\text{Pb}$ , the smallest measured angle was  $10.4^\circ$  in the c.m. system. At angles smaller than  $5^\circ$  (c.m.), the cross section is more than one order of magnitude larger than at  $10^\circ$ . The lack of data between  $0^\circ$  and  $10^\circ$  resulted in Legendre fits that did not give a good description of the angular distribution, e.g., the minimum around  $14^\circ$  was poorly reproduced. Therefore, three points measured by Salmon at 96 MeV [21] [at  $3.01$ ,  $5.02$ , and  $7.54^\circ$  (c.m.)] were added to our  ${}^{208}\text{Pb}$  distribution before performing the Monte Carlo simulations. For this purpose, the Salmon c.m. data were first converted to the laboratory system, and the cross section values were slightly modified to simulate that they had been measured with SCANDAL. A successful reproduction of the values stated in Ref. [21], after having done the Monte Carlo simulations, demonstrated the consistency of the initial modification of the Salmon data.

Finally, the  ${}^{208}\text{Pb}(n, n)$  angular distribution was corrected for the  ${}^{206}\text{Pb}$  contribution in the scattering target. This was done using the ratio between the theoretical neutron elastic scattering cross sections for  ${}^{206}\text{Pb}$  and  ${}^{208}\text{Pb}$ , calculated with the global potential by Koning and Delaroche [30]. The correction was less than 1%.

The absolute normalization of the data was obtained from knowledge of the total elastic cross section  $\sigma_{EL}$ , which was determined from the difference between the total cross section  $\sigma_T$  [10] and the reaction cross section  $\sigma_R$  [42,43]. This  $\sigma_T - \sigma_R$  method, which is expected to have an uncertainty of about 3%, was used to normalize the  ${}^{12}\text{C}$  data. The values used for  $\sigma_T$  and  $\sigma_R$  for  ${}^{12}\text{C}$  were  $512 \pm 3$  mb and  $226 \pm 5$  mb, respectively. The  $\sigma_T$  value was a weighted average of two data points at 95.2 and 96.2 MeV. The  $\sigma_R$  value was obtained from a weighted average of five measurements at 95 MeV in Ref. [42] and from two measurements in Ref. [43], at 81 and 105 MeV. This gave the normalized experimental value  $\sigma_{EL} = 286 \pm 7$  mb.

The  ${}^{208}\text{Pb}(n, n)$  data were normalized relative to the present  ${}^{12}\text{C}(n, n)$  data, knowing the relative neutron fluences, target masses, etc.; giving an experimental total elastic cross section of  $2764 \pm 51$  mb for  ${}^{208}\text{Pb}$ . This value has previously been determined with the  $\sigma_T - \sigma_R$  method, using  $\sigma_T = 4654 \pm 47$  mb and  $\sigma_R = 1810 \pm 70$  mb, resulting in  $\sigma_{EL}$

TABLE II. Differential cross sections for elastic neutron scattering at 96 MeV. The total statistical errors in columns “ $\Delta d\sigma/d\Omega$ ” include random errors constituted by counting statistics and contributions from the multiple scattering corrections, while columns “ $\Delta_{\text{rel.}}$ ” show the relative statistical errors in the experiment before these corrections are made. The columns “ $\Delta_{\text{ang.}}$ ” refer to cross section uncertainty due to the angle uncertainty in the measurement as described in the text.

$\theta_{\text{c.m.}}$ (deg)	$^{208}\text{Pb}(n, n)$				$\theta_{\text{c.m.}}$ (deg)	$^{12}\text{C}(n, n)$			
	$d\sigma/d\Omega$ (mb/sr)	$\Delta d\sigma/d\Omega$ (mb/sr)	$\Delta_{\text{rel.}}$ (%)	$\Delta_{\text{ang.}}$ (mb/sr)		$d\sigma/d\Omega$ (mb/sr)	$\Delta d\sigma/d\Omega$ (mb/sr)	$\Delta_{\text{rel.}}$ (%)	$\Delta_{\text{ang.}}$ (mb/sr)
10.4	3764	46	0.8	1835	11.2	743	10	1.3	81
13.9	1281	26	1.5	228	14.9	522	8	1.5	75
17.7	989	18	1.6	100	19.0	240	5	2.1	41
21.7	402	12	2.4	145	23.4	122	4	2.8	23
25.7	187.1	9.7	3.5	15.3	27.7	54.4	2.9	4.7	10.3
29.5	165.3	7.5	3.6	22.7	31.7	23.9	1.9	6.5	3.8
30.0	145.0	6.4	3.5	25.2	32.3	15.7	1.5	7.6	2.4
33.4	74.0	5.4	5.3	21.3	35.9	11.3	1.3	9.3	1.4
34.4	44.7	4.6	5.9	9.3	36.9	9.7	1.2	10	1.2
37.6	36.1	3.6	6.8	2.0	40.3	6.0	1.0	13	0.7
38.7	38.1	3.2	7.4	0.4	41.5	5.2	0.9	15	0.6
41.9	28.6	2.6	9.3	6.1	44.9	3.8	0.9	18	0.5
43.2	21.9	2.5	8.9	5.5	46.3	2.9	0.8	19	0.4
46.3	9.6	1.6	12	0.4	49.5	1.8	0.6	23	0.3
47.2	13.2	1.7	12	0.1	50.5	0.3	0.3	56	0.1
50.3	7.9	1.3	15	0.7	53.8	0.9	0.5	41	0.1
51.0	9.9	1.7	13	1.1	54.5	0.6	0.4	41	0.1
54.6	4.3	1.1	22	1.1	58.3	0.8	0.4	36	0.1
54.9	5.2	0.9	15	1.2	58.6	0.8	0.3	33	0.1
59.3	2.9	0.8	26	0.1	63.2	0.3	0.2	58	0.0
63.6	1.4	0.6	43	0.4	67.6	0.1	0.2	131	0.0
67.2	0.5	0.6	66	0.1	71.3	0.4	0.2	49	0.0
71.2	1.2	0.6	52	0.1					

$=2847 \pm 84$  mb, i.e., 3.0% from our value. The  $\sigma_T$  value for  $^{208}\text{Pb}$  was a weighted average of ten data points around 96 MeV. The spread of these points was significantly larger than their respective errors, and as a result of a new estimation, an error of 1% was assumed [44]. The  $\sigma_R$  value was obtained from a weighted average of two measurements at 95 MeV in reference [42], and from two measurements in reference [43], at 81 and 105 MeV.

### E. Estimation of experimental uncertainties

The strategy of the present experiment has been to obtain a set of relative differential cross section data, which is finally normalized using previously known information, as described above. With such an approach, inefficiencies that affect all data points by the same amount, such as drift chamber inefficiencies or computer dead time, are taken care of by the normalization procedure. Inefficiencies which are angle dependent, but can be determined or modeled with reasonably good precision, are not very detrimental. For instance, the losses due to nuclear reactions differ slightly for different CsI detectors, because the amount of material in front of them varies due to geometry. These losses can, however, be modeled rather well, making the total uncertainty

after correction insignificant. The most difficult type of uncertainties are the ones that affect the shape of the angular distributions in a random way. The random error is due to counting statistics and includes the contribution from the background subtraction. It varies significantly with the scattering angle, due to the steepness of the cross sections.

The correction (<6%) for the contribution from the low-energy continuum of the  $^7\text{Li}(p, n)$  spectrum to the  $np$  scattering peak introduces a systematic uncertainty that varies with the peak width. Assuming a relative uncertainty of 10% in the correction, an error in the data of at most 0.6% arises. This means that the point-to-point uncertainty is completely dominated by the random error coming from counting statistics regardless of scattering angle.

The Monte Carlo simulation adds a statistical error to the point-to-point uncertainty. The total statistical errors, including both these contributions, are calculated in the program and given as output together with the corrected angular distributions. The results are listed in Table II. In addition to the total errors, Table II shows (for the respective scattering target) the relative statistical errors in the measurements, i.e., before corrections were made.

The cross section ratios linking the heights of the Gaussians for the first excited states and the ground states in the

spectrum functions (established to define the integration interval  $\pm\Gamma$ ) affect the fraction of the integrated number of events that should be ascribed to elastic scattering. By varying the calculated relations between the excited states and the ground states, with an estimated uncertainty of  $\pm 30\%$  of the cross sections for excitation of the low-lying excited states, it was found that the uncertainties in the final elastic cross sections changed with 1% or less for most of the angular range, because of the relatively weak excitation of the low-lying excited states. At large angles for  $^{12}\text{C}$ , the 4.4.-MeV state is about as strongly excited as the ground state, and in this case the uncertainty in the elastic cross section is up to 4% due to this effect. At these large angles, however, the statistical uncertainties are much larger. Therefore this contribution was ignored.

The fitting procedure itself produces an uncertainty in the resolution  $\Gamma$ . As the resolution is used to determine the interval for integration of the elastic scattering events, it also contributes to the point-to-point error in the angular distribution. This effect was examined by varying the integration intervals using the uncertainty in  $\Gamma$ . It was found that the errors in the cross section typically increased with up to 5% (e.g., a 10.0% error becoming a 10.5% error). At a few angles with poor statistics this figure was doubled.

The positive effect of the lead collimator varies with the elastic neutron scattering angle, as defined by the positions of the real scattering target and the CsI detector. For the detectors at small angles, the angles of neutrons scattered in the target and in the upstream fission detector are approximately equal, with a large elastic scattering cross section. The usefulness of the collimator is moderate because of a relatively short path length for the neutrons passing it (coming from the fission detector).

For detectors placed at the largest angles, the collimator effect is also moderate, while the angles of neutrons scattered in the fission monitor are smaller than those of neutrons scattered in the real target. This means that the cross section is larger for the unwanted neutrons. On the other hand, all neutrons are assumed to originate from the target, and with a maximum converter scattering angle criterion of  $10^\circ$ , the calculated neutron energy is approximately equal to the detected proton energy. For neutrons coming from the fission monitor, with conversion angles being in reality much larger than  $10^\circ$ , this means that the calculated neutron energies are too small and the obtained excitation energies too high; i.e., these events are prevented from contaminating the ground state peaks at 0 MeV.

For detectors at intermediate angles, the elastic scattering cross section is still larger for neutrons coming from the fission detector. At the same time, the effect of removing such events from the ground state peaks by assigning too high excitation energies is smaller than at extremely large angles. Fortunately, this is at the same time the angular region where the attenuation in the collimator is at its maximum.

In all cases, background subtraction removes the unwanted events. The purpose of the collimator is to reduce the statistical uncertainties.

The angular dependence of the neutron attenuation in the collimator can be illustrated by comparing background runs with and without the collimator (normalized to the same neutron fluence). It was found that for a CsI detector at  $10^\circ$ , around 40% of the background events were removed, while at  $25^\circ$ , this fraction had increased to 80%. At  $45^\circ$ , the level was back at 40%.

The angular resolution depends on the width of the scattering target. To estimate this resolution, the  $^{208}\text{Pb}$  and  $^{12}\text{C}$  targets were divided into a number of volume pixels, and the rms value of the elastic scattering angle distribution, coming from the target pixels of events detected in one specific converter pixel, was calculated. This was done for all pixels in the region of interest in the converter, giving an average value per detector in the  $1.0^\circ - 1.3^\circ$  (rms) range.

When measuring a differential cross section with a pronounced angular dependence, such as for  $^{208}\text{Pb}(n, n)$ , even small uncertainties in the angular information can produce significant uncertainties in the result. The angular uncertainties in the present experiment are dominated by the limited knowledge of the positions of the target and the drift chambers. Both these are known to slightly better than 1 mm, resulting in an angular uncertainty of about  $1^\circ$ . This uncertainty results in an equal shift of all 12 data points produced by the same SCANDAL arm. In addition, the drift chambers contain many drift cells, which work as physically independent detectors, each with its own TDC for time recording. Imperfect time calibration of these TDCs can produce conversion position errors of up to about 0.5 mm, which corresponds to about  $0.5^\circ$  shift of the presumed scattering angle. This uncertainty is randomly distributed among the data points.

The uncertainty in scattering angle produces a significant cross section uncertainty, because the cross section varies rapidly with angle. We have used the "best fit" to data in Sec. IV to estimate this effect, i.e., we have investigated how much the cross section varies over the angular range covered by each CsI. For most of the angular range studied, this effect is larger than the statistical uncertainty, and it is generally much larger for  $^{208}\text{Pb}$  than  $^{12}\text{C}$  because of the more rapid variation of the  $^{208}\text{Pb}$  cross section.

#### IV. RESULTS AND DISCUSSION

Angular distributions of elastic neutron scattering from  $^{208}\text{Pb}$  and  $^{12}\text{C}$  at 96 MeV incident neutron energy are presented in Figs. 5 and 6, where they are compared with phenomenological and microscopic optical model calculations. The number of data points in the  $^{208}\text{Pb}(n, n)$  distribution is 23, since one of the CsI detectors was excluded because of malfunctioning. This is not a major problem, as the detector belonged to the angular region covered by both SCANDAL arms, and a detector on the other arm was placed at the same scattering angle. The  $^{12}\text{C}(n, n)$  distribution has 22 data points because, in addition to the malfunctioning detector, the statistics in the CsI crystal at the largest scattering angle were too poor.

With the malfunctioning CsI crystal removed, the overlapping angular range comprises seven pairs of detectors at

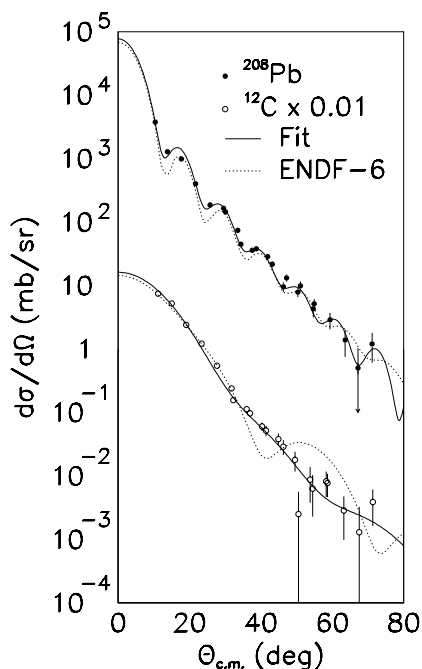


FIG. 5. Angular distributions of elastic neutron scattering from  $^{12}\text{C}$  (open circles) and  $^{208}\text{Pb}$  (solid circles) at 96 MeV incident energy. The  $^{12}\text{C}$  data and calculations have been multiplied by 0.01. The solid lines represent best fits to the present data, using the parametrization by Koning and Delaroche [30], while the dotted lines are cross sections given by the evaluated nuclear data file ENDF-6 [45]. See the text for details.

nearly the same angles. The level of agreement between the measurements with the two arms was examined by calculating the reduced  $\chi^2$  between the two sets. Since the detectors in each pair were not placed exactly at the same angle, the points were put on the same footing by subtracting an optical model prediction of the cross section from the experimental value at the respective angle. After this, the average difference between the two data points in the respective pair was calculated to be  $1.4\sigma$  in the case of  $^{208}\text{Pb}$  and  $1.0\sigma$  for  $^{12}\text{C}$ . The reduced  $\chi^2$  when comparing the full ensemble of data points between the two arms in the overlapping range was 1.3 for  $^{208}\text{Pb}$  and 1.6 for  $^{12}\text{C}$ .

The fact that  $\chi^2$  is larger than 1.0 when comparing the two arms indicates the presence of systematic uncertainties not taken into account. One known systematic effect is due to the angular precision. Since the cross section varies dramatically with angle, even an angular error within the small angular uncertainty can result in a cross section mismatch sufficiently large to cause these effects. The fact that  $\chi^2$  is not much larger than 1.0 implies that the systematic uncertainties are comparable in magnitude with the statistical errors.

In Fig. 5, the data are compared with fits to the present data that use a recent parametrization of the phenomenological optical model potential (OMP) by Koning and Delaroche [30] (solid curves). These are of a best-fit type, i.e., representing a potential for the respective nucleus and the incident neutron energy only. Comparisons are also made with the cross sections given by the evaluated nuclear data files in the ENDF/B-VI library, Release 6 (ENDF-6) [45] (dotted

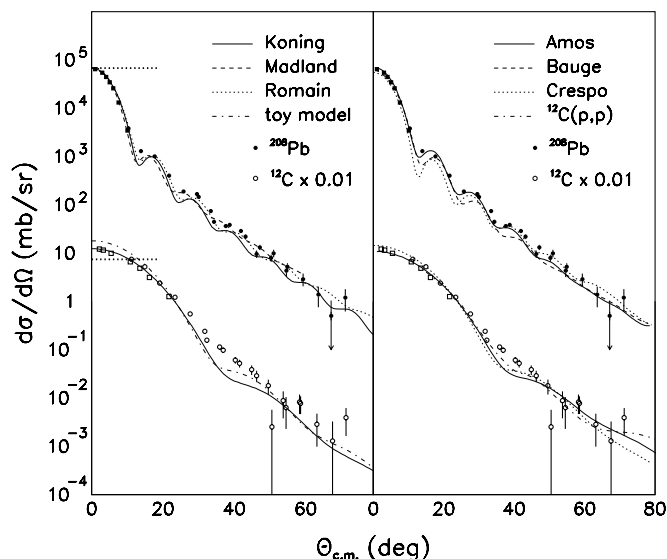


FIG. 6. Angular distributions of elastic neutron scattering from  $^{12}\text{C}$  (open circles) and  $^{208}\text{Pb}$  (solid circles) at 96 MeV incident energy. The  $^{12}\text{C}$  data and calculations have been multiplied by 0.01. The data of Salmon at 96 MeV [21] are shown as squares. Left panel: predictions of Koning and Delaroche (solid) [30], of Madland and Kozack (dashed) [47], of Romain and Delaroche (dotted) [50], and of a modified version (dash-dotted) of the model of Koning and Delaroche. The thick dotted horizontal lines show Wick's limit for the two nuclei. Right panel: predictions by Amos, Deb, and Karataglidis (solid) [52], of Bauge, Delaroche, and Girod (dashed) [54], and of Crespo and Moro (dotted) [56], as well as data on elastic proton scattering from  $^{12}\text{C}$  [57] (dash-dotted). See the text for details.

curves). The error bars on the SCANDAL data are the total statistical errors listed in Table II, including the random errors constituted by counting statistics and the additional statistical errors added by the Monte Carlo simulations.

When scrutinizing the  $^{208}\text{Pb}$  data in Fig. 5, it can be seen that two data points, at  $14^\circ$  and  $18^\circ$ , lie significantly above and below the fit, respectively. This is most likely due to an imperfect correction for multiple scattering. The large size of the target makes multiple scattering a relatively important phenomenon. Multiple scattering tends to fill minima and reduce maxima in the angular distribution. Corrections for this rely heavily on the cross section information at small angles ( $0^\circ$ – $10^\circ$ ), where data are missing in the present experiment. In addition, precise data around the first minimum and second maximum are important for a proper correction.

In the fit to all  $^{208}\text{Pb}$  data in Fig. 5, the reduced  $\chi^2$  is very large, i.e., around 15. When removing the data points at  $14^\circ$  and  $18^\circ$  discussed above, the reduced  $\chi^2$  decreases to 1.5. A major uncertainty not included in these fits is the angular precision. Due to the steepness of the  $^{208}\text{Pb}$  angular distribution, even a minor angular shift corresponds to a large change in cross section. At around  $10^\circ$  scattering angle, a shift of  $0.5^\circ$ , i.e., within the angular precision, changes the cross section by about 40%. This makes it not very meaningful to compare  $\chi^2$  of various fits on an absolute scale. Relative comparisons can still be informative, although minor differences should not be overemphasized.

The fit in Fig. 5 to the  $^{12}\text{C}$  data results in a reduced  $\chi^2$  of 6.8. If removing the datum at  $11^\circ$  or shifting it by less than  $1^\circ$  towards larger angles,  $\chi^2$  per degree of freedom reduces to about 3. It is not surprising that the  $^{12}\text{C}$  produces better fits without removing data points. The cross section as such is less steep and contains less structure, and its lower absolute magnitude results in much less multiple scattering.

In Fig. 6, the data are compared with phenomenological and microscopic optical model predictions in the left and right panels, respectively. The theoretical curves have all been folded with the experimental angular resolution to facilitate comparisons with data. The data of Salmon at 96 MeV [21] are also included.

Predictions by a phenomenological global OMP of Koning and Delaroche [30] are given by the solid curves in the left panel of Fig. 6. This global OMP is valid for incident nucleon energies between 1 keV and 200 MeV and masses from 24 to 209. It is based on a smooth functional form for the energy dependence of the potential depths, and on physically constrained geometry parameters. An extensive collection of experimental datasets for different types of observables was used to determine the parameters of this OMP.

The dashed line in the left panel of Fig. 6 shows the result of a scattering calculation performed in 1990 by Kozack and Madland [47], using their global nucleon-nucleus intermediate energy Dirac phenomenological optical potential for  $^{208}\text{Pb}$  [48]. The potential contains scalar and vector terms, based upon the Walecka model [49], and includes isospin dependence through a relativistic generalization of the Lane model [2]. The isospin dependence was determined by simultaneous least-squares adjustment with respect to measured proton elastic scattering and neutron total cross section observables. Symmetrized Saxon-Wood form factors are used, and the potential contains a total of 20 parameters to describe nucleon scattering by  $^{208}\text{Pb}$  in the energy range 95–300 MeV.

An OMP calculation by Romain and Delaroche [50], based on a dispersive OMP approach treating non-locality in a manner similar to that of Buck and Perey [51] for energy dependencies, is presented as the dotted line in the left panel of Fig. 6.

Amos, Deb and Karataglidis have developed a microscopic ( $g$ -folding) prescription for the optical potentials [25,52], where a complete  $(0+2)\hbar\omega$  model of the structure of  $^{12}\text{C}$  and a Skyrme-Hartree-Fock model for  $^{208}\text{Pb}$ , have been used in the foldings. The predictions, presented as the solid line in the right panel of Fig. 6, were obtained employing the effective (medium modified)  $NN$  interaction based upon the Bonn-B interaction [53].

Bauge, Delaroche, and Girod have developed a Lane-consistent, semimicroscopic OMP [54], which is built by folding radial matter densities from a Hartree-Fock-Bogoliubov calculation (using the Gogny D1S effective interaction) with an OMP in nuclear matter that is based on an extension of that of Jeukenne, Lejeune, and Mahaux [55]. The result is presented as the dashed line in the right panel of Fig. 6. This extended OMP features strong renormalizations

of its isovector components, and has recently been tested extensively against  $(p, p)$  and  $(n, n)$  data, as well as  $(p, n)$  IAS data [54].

Finally, Crespo and Moro have made a prediction [25], shown as the dotted line in the right panel of Fig. 6, where the elastic observable was generated by a multiple scattering expansion of the optical potential in terms of the free  $NN$  transition amplitude, calculated in the single scattering, “ $t\rho$ ,” approximation [56]. In the description of the target nucleus, there is no distinction between protons and neutrons. For  $^{12}\text{C}$ , the matter density distribution is deduced directly from the harmonic-oscillator shell model, with  $b=1.55$  fm. In the case of  $^{208}\text{Pb}$ , a two-parameter Fermi matter density distribution with half-density radius  $c=6.624$  fm and diffuseness  $a=0.549$  fm has been used.

When comparing these predictions with data, a few striking features are evident. All models are in reasonably good agreement with the  $^{208}\text{Pb}$  data. It should be pointed out that none of the predictions in Fig. 6 contain parameters adjusted to the present experiment. In fact, they were all made before data were available. The level of agreement between models and data for  $^{208}\text{Pb}$  have been inspected by computing  $\chi^2$ . For this exercise, only the uncertainties due to counting statistics have been used.

A normalization error can produce a major  $\chi^2$  contribution. Therefore, it was tested to renormalize all theories to produce a minimum  $\chi^2$ . The absolute  $\chi^2$  values were significantly reduced for all models by this procedure. In addition, the two data points at  $14^\circ$  and  $18^\circ$  were removed from this comparison, since there are good reasons to believe that they are imperfectly corrected for multiple scattering (as has been discussed above), and will therefore produce artificially large  $\chi^2$  contributions. The result of this test is that the ENDF-6 and Romain *et al.* predictions require very little renormalization, below 5%, while Madland *et al.* and Crespo *et al.* need about 30% renormalization. For the other models, the optimum renormalization is around 10%. The resulting  $\chi^2$  values are 2.0 for the Amos *et al.* model and around 10 for the others.

Without renormalization, the values are dramatically larger, to the extent that the absolute numbers are meaningless, but relative comparisons might still be of some value. The models by Amos *et al.* and Romain *et al.* have the lowest  $\chi^2$ , with the Bauge *et al.* and Koning *et al.* models, as well as the ENDF-6 prediction, in a second group. It should be pointed out, however, that the results are not dramatically different for the various models. That the Amos *et al.* and Romain *et al.* models are in best agreement is not surprising, because they are single-nucleus models, while models with a larger range of validity give a less perfect description for a particular nucleus. The Madland *et al.* model was determined by simultaneously fitting a large proton dataset and a small neutron dataset (mostly total cross sections). For such a procedure, the agreement is surprisingly good. A general observation is also that all models are 0–30% below the data. No model exceeds the measured angular distribution.

It should be pointed out that essentially all models reproduce the experimental total elastic cross section fairly well without renormalization. The Crespo *et al.* model presents a

total elastic cross section which is 30% lower than the experimental value. All the other models are less than 10% lower than the experimental value, while no model exceeds it. After renormalization with the prescription above, i.e., fitting to the present dataset, all models describe the experimental total elastic cross section to within 10%. Thus, it seems as the largest discrepancies between data and theory models are related to the absolute normalization rather than to differences in the shape of the angular distribution.

All models, as well as the ENDF-6 data shown in Fig. 5, fail to describe the  $^{12}\text{C}$  data in the  $30^\circ$ – $50^\circ$  range. The models and the evaluation predict a saddle structure, which is not evident from the data. The reason for this mismatch might be that there are target correlations other than the Pauli principle, or other nuclear structure effects, that are not included in the theoretical models. Also, if the  $^{12}\text{C}$  nucleus matter distribution has a more diffuse edge than anticipated, the predicted structure could be washed out. In addition to the mismatch between  $30^\circ$  and  $50^\circ$ , the ENDF-6 prediction shows a maximum at even larger angles that is not supported by the data. It can be noted that proton scattering data on  $^{12}\text{C}$  at 95 MeV [57], which should agree with our data if isospin were a good symmetry, are closer to our data than the predictions of every model. The disagreement between models and  $^{12}\text{C}$  data should not be overemphasized though. Models which presume mean-field properties of nuclei to be dominant can have problems describing  $^{12}\text{C}$  data, because surface effects are very important in  $^{12}\text{C}$ .

The models above are all valid for spherical nuclei. It is known, however, that  $^{12}\text{C}$  to a significant degree displays properties of a three- $\alpha$  cluster. Coexistence of such a structure with a spherical shape might result in a matter distribution with a more diffuse edge than anticipated by the spherical models, and thus the predicted structure could be washed out.

We have developed a toy model to investigate this hypothesis. The increased effective radius of the  $^{12}\text{C}$  ground state due to three- $\alpha$  cluster effects has been studied theoretically for proton elastic scattering, however, at higher energies [58]. We have modified the global model of Koning and Delaroche, using the parameters of Ref. [58], to obtain a new radius  $R$  and a new potential depth  $V$ , presuming  $VR^2$  fixed, and keeping the diffuseness unchanged. As can be seen in the left panel of Fig. 6 (dash-dotted curve), the elastic neutron scattering cross section calculated with these modifications moves closer to the data in the  $30^\circ$ – $50^\circ$  range, but at the expense that the description gets worse at small angles.

The OMP results can be inspected in Table III. A few striking features are evident. For  $^{208}\text{Pb}$ , the best-fit solution seems to indicate a deeper central potential than the global model result, and the surface term is stronger as well. For  $^{12}\text{C}$ , it is notable that the best fit to data agree rather well with the toy model. Both have a shallower central potential than the global spherical potential, and the central radius is larger. Thus, the best-fit solution seems to be at least as close to a solution based on a three- $\alpha$  cluster structure of  $^{12}\text{C}$  as to a spherical shape. It should be pointed out, however, that this

TABLE III. Optical model parameters from the potential of Koning and Delaroche [30]. Parameters for the global optical potential are compared with best-fit values obtained for our angular distributions at 96 MeV. For  $^{12}\text{C}$ , parameters of a toy model used to investigate possible contributions from three- $\alpha$  cluster effects are also shown. See the text for details.

OMP parameter	$^{208}\text{Pb}(n, n)$		$^{12}\text{C}(n, n)$		Toy
	Global	Best fit	Global	Best fit	
$V_V(E)$	22.530	25.501	26.300	21.797	21.830
$W_V(E)$	8.790	6.627	8.350	4.754	6.930
$r_V$	1.235	1.187	1.127	1.264	1.240
$a_V$	0.647	0.778	0.676	0.743	0.676
$W_D(E)$	1.990	4.182	1.540	1.000	1.280
$r_D$	1.248	1.303	1.306	1.333	1.437
$a_D$	0.510	0.164	0.543	0.400	0.543
$V_{SO}(E)$	4.360	4.099	3.880	5.603	3.220
$W_{SO}(E)$	-0.890	-0.890	-0.960	-0.890	-0.800
$r_{SO}$	1.076	1.151	0.903	0.849	0.993
$a_{SO}$	0.590	0.680	0.590	0.507	0.590

should only be seen as an indication of a possible cause of the effect, since the model is too simplified to allow quantitative conclusions.

A basic feature of the optical model is that it establishes a lower limit on the differential elastic scattering cross section at  $0^\circ$  if the total cross section is known

$$\frac{d\sigma(0^\circ)}{d\Omega} \geq \left( \frac{\sigma_T}{4\pi\lambda} \right)^2,$$

often referred to as Wick's limit [59,60]. For most neutron scattering experiments below 30 MeV, it has been found that the  $0^\circ$  cross section is very close to the limit [61,62]. This observation has led to the suggestion that in the absence of a good experimental normalization, Wick's limit could be treated as an equality for normalization of elastic scattering data [63]. However, there is no *a priori* reason why the cross section cannot exceed the limit significantly. An interesting observation in the present experiment is that the  $^{208}\text{Pb}$  data are in good agreement with Wick's limit, while the  $^{12}\text{C}$   $0^\circ$  cross section lies about 70% above the limit. This could not be due to normalization problems only, because the  $^{208}\text{Pb}$  data are measured relative to the  $^{12}\text{C}$  data. Thus, if lowering the  $^{12}\text{C}$  cross section to be close to Wick's limit, the  $^{208}\text{Pb}$  data would fall below the limit, which is strictly forbidden. A similar behavior has previously been observed in neutron elastic scattering at 65 MeV [17], where the C data overshoot Wick's limit by about 30%, while the data on Si, Ca, Sn, and Pb agree with the limit. A follow-up experiment on the  $^{12}\text{C}$  cross section at  $0^\circ$  is under analysis [46].

One of the applications benefitting from the  $^{12}\text{C}(n, n)$  measurement presented here is fast-neutron cancer therapy. In radiation treatment with fast neutrons, the energy is transferred from the neutron to tissue in two stages. In the first stage, the neutron interacts with a nucleus, which can result in a wide range of secondary charged particles or in a heavy

recoil of the target nucleus due to elastic neutron scattering. The second stage involves the transfer of energy from the secondary charged particles or from the recoiling nucleus, to the tissue through excitation and ionization. The quantity kerma—kinetic energy released in matter—is used to describe the interaction in the first stage. It corresponds to the kinetic energy released by the primary neutrons per unit mass in the form of secondary particles or recoiling nuclei. Furthermore, the kerma coefficient is the kerma per unit neutron fluence.

Partial neutron kerma coefficients, i.e., the kerma for production of a specific charged particle per unit neutron fluence, or for the recoil of the nucleus in case of elastic scattering, can be obtained directly from the measured microscopic cross sections. The elastic recoil kerma coefficient is defined by

$$k_{EL} = N \int E \frac{d\sigma}{d\Omega}(\theta) 2\pi \sin \theta d\theta, \quad (1)$$

where  $N$  is the number of target nuclei per mass unit,  $E$  is the energy of the recoiling  $^{12}\text{C}$  nucleus, and  $2\pi \sin \theta d\theta$  is the solid angle element corresponding to the scattering angle  $\theta$ . This gives an experimental elastic recoil kerma coefficient of  $k_{EL} = 0.126 \pm 0.009$  fGy  $\text{m}^2$  for  $^{12}\text{C}$  at 96 MeV, where the uncertainty has contributions from counting statistics and from the absolute normalization of the cross section. The elastic scattering cross section values were taken from a Legendre polynomial fit to our data, covering the full angular range ( $0^\circ$ – $180^\circ$ ). It should be pointed out that 90% of the contributions to the elastic recoil kerma coefficient comes from the angular range  $10$ – $70^\circ$ , i.e., the range covered by SCANDAL.

Our value can be compared with the evaluated elastic recoil kerma coefficient  $0.132$  fGy  $\text{m}^2$  given in Ref. [64]. This reference gives evaluated cross section data in the ENDF-6 format for neutrons from 20 to 150 MeV, generated with nuclear model calculations and with measurements up to 70 MeV used as benchmarks; and kerma coefficients that were derived from these cross sections. The Los Alamos GNASH model code [65] was used for this purpose, along with the optical model codes ECIS [66] and SCAT [67]. The estimated uncertainty in the calculations for carbon at 100 MeV is  $\approx 10\%$ .

The elastic recoil kerma coefficient has also been calculated from the cross section prediction by the global OMP of Koning and Delaroche, by the microscopic calculations of Amos, Deb, and Karataglidis, and by Crespo and Moro; using Eq. (1). The values were lower than the ones above;  $0.097$  fGy  $\text{m}^2$ ,  $0.107$  fGy  $\text{m}^2$ , and  $0.115$  fGy  $\text{m}^2$ , respectively. This can be understood from the fact that the predicted cross sections have a saddle structure between  $30^\circ$  and  $50^\circ$  (see above), while the measured cross section is larger in this region. The evaluated  $k_{EL}$  value ( $0.132$  fGy  $\text{m}^2$ ) is closest to our measurement, but this agreement is accidental, since the saddle structure in the evaluated cross section is compensated for by the maximum at angles larger than  $50^\circ$ .

## V. SUMMARY, CONCLUSIONS, AND OUTLOOK

First results on elastic neutron scattering from  $^{12}\text{C}$  and  $^{208}\text{Pb}$  at 96 MeV incident neutron energy have been presented and compared with theory predictions. This experiment represents the highest neutron energy where the ground state has been resolved from the first excited state in neutron scattering. The measured cross sections span more than four orders of magnitude. Thereby, the experiment has met—and surpassed—the design specifications.

The overall agreement for  $^{208}\text{Pb}$  with predictions from theoretical models, both phenomenological and microscopic, is good. In particular, the agreement in absolute cross section scale is impressive. It can therefore be concluded that the theories describing this spherical, double-magic nucleus are under reasonable control. For  $^{12}\text{C}$ , on the other hand, significant differences have been demonstrated between predictions and experiment. Possible explanations might be that  $^{12}\text{C}$  exhibits surface effects and deformations coming from a three- $\alpha$  cluster structure. Another effect, such as a more diffuse edge than anticipated, may also play a role. These contributions have not been taken into account in the model calculations presented here, and therefore it is not surprising that the description of the  $^{12}\text{C}$  data is poor in the  $30^\circ$ – $50^\circ$  range. This defectiveness is also found in the evaluated (ENDF-6) cross section, which might call for a reevaluation in the future.

The absolute normalization of the angular distribution for  $^{12}\text{C}$  was obtained from knowing the total elastic cross section  $\sigma_{EL}$ , which was determined from the difference between the total cross section  $\sigma_T$  and the reaction cross section  $\sigma_R$ . After that, the  $^{208}\text{Pb}(n, n)$  data were normalized relative to the  $^{12}\text{C}(n, n)$  data. To the best of our knowledge, this method has never been used before to normalize elastic neutron scattering cross sections. The estimated uncertainty, 3%, is comparable with what can be achieved with other methods for absolute normalization of neutron-induced cross sections, i.e., tagging or combination of total and elastic  $np$  scattering. It can, however, only be used for a few nuclei because reaction cross sections are known only for a few nuclei and energies.

Before long, a second, independent, normalization of the angular distributions for  $^{208}\text{Pb}(n, n)$  and  $^{12}\text{C}(n, n)$  will be performed, based on relative measurements versus the  $np$  scattering cross section. A recent high-precision measurement of  $np$  scattering at 96 MeV in the  $74^\circ$ – $180^\circ$  range claims an absolute uncertainty of 1.9% [68], but this is mostly outside our angular range. However, in addition to this, a relative measurement of the angular distribution of  $\text{H}(n, n)$  from (close to) zero degrees and out to angles overlapping with the existing data has been done with SCANDAL, and is under analysis [46]. Thereby, a full angular distribution is available, and thus a normalization to the total cross section, having a very small uncertainty (about 1%), can be made. The angle-integrated elastic scattering cross section accounts for more than 99% of the total cross section, with very small corrections for capture and bremsstrahlung processes.

The  $\text{H}(n, n)$  cross section was measured in a  $\text{CH}_2$ -vs- $\text{C}$  difference measurement. This allows us to normalize the  $\text{C}(n, n)$  cross section to the  $\text{H}(n, n)$  primary standard cross section, and thus the  $\text{C}(n, n)$  cross section can be established

as a secondary standard, allowing all other nuclei to be measured relative to  $C(n, n)$ . This will also allow a stringent test of the  $\sigma_T - \sigma_R$  normalization method used in the present work.

A new determination of the medically important elastic recoil kerma coefficient has been presented for  $^{12}\text{C}$  at 96 MeV. The present value and the evaluation [64] are in good agreement, but this has been found to be accidental. The evaluated elastic cross section deviates significantly from the experimental data, but in such a way that the deviations compensate each other. This gives further support for a renewed evaluation.

The  $^{16}\text{O}(n, n)$ ,  $^{56}\text{Fe}(n, n)$ , and  $^{89}\text{Y}(n, n)$  cross sections have also been measured with SCANDAL, and data are under analysis [69–71]. These nuclei were chosen, together with  $^{208}\text{Pb}$ , in order to study the behavior of elastic scattering in a more general way, i.e., for magic or double-magic nuclei over a broad mass range. The measurements at 96 MeV provide important input to the development of the optical model, not the least because of the lack of elastic neutron scattering data above 20 MeV. A possible development would be to go further up in energy [30]. The maximum energy that can be delivered by the neutron beam facility at

the The Svedberg Laboratory (TSL) in Uppsala is 180 MeV, and the performance of SCANDAL indicates that it would be feasible to detect elastic neutron scattering at this energy, assuming that some changes are made in the detector hardware.

A relatively small effort, however, would be to move a SCANDAL arm downstream and thereby reduce the smallest scattering angle from  $10^\circ$  to  $3^\circ$ . One experimental campaign could be dedicated to such a small-angle measurement, covering several target nuclei.

#### ACKNOWLEDGMENTS

We wish to thank the technical staff of the The Svedberg Laboratory for enthusiastic and skillful assistance. We are also very grateful to Siebren van der Werf and to Valentin Corcalciuc for their computational aid. This work was supported by the HINDAS project of the 5th EU framework programme, as well as by Vattenfall AB, Swedish Nuclear Fuel and Waste Management Company, Swedish Nuclear Power Inspectorate, Barsebäck Power AB, Ringhals AB, Swedish Defence Research Agency, and the Swedish Research Council.

- 
- [1] *Neutron-Nucleus Collisions: A Probe of Nuclear Structure*, edited by J. Rapaport, R. W. Finlay, S. M. Grimes, and F. S. Dicitrich, AIP Conf. Proc. No. 124 (AIP, New York, 1985).
- [2] A. M. Lane, Nucl. Phys. **35**, 676 (1962).
- [3] C. R. Chinn, Ch. Elster, and R. M. Thaler, Phys. Rev. C **48**, 2956 (1993).
- [4] T. N. Taddeucci, C. A. Goulding, T. A. Carey, R. C. Byrd, C. D. Goodman, C. Gaarde, J. Larsen, D. Horen, J. Rapaport, and E. Sugarbaker, Nucl. Phys. **A469**, 125 (1987).
- [5] A. Koning, H. Beijers, J. Benlliure, O. Bersillon, J. Blomgren, J. Cugnon, M. Duijvestijn, Ph. Eudes, D. Filges, F. Haddad, S. Hilaire, C. Lebrun, F.-R. Lecolley, S. Leray, J.-P. Meulders, R. Michel, R.-D. Neef, R. Nolte, N. Olsson, E. Ostendorf, E. Ramström, K.-H. Schmidt, H. Schuhmacher, I. Slypen, H.-A. Synal, and R. Weinreich, J. Nucl. Sci. Tech., Suppl. **2**, 1161 (2002).
- [6] A. Wambersie, P. Pihet, and H. G. Menzel, Radiat. Prot. Dosim. **31**, 421 (1990).
- [7] H. H. K. Tang, IBM J. Res. Dev. **40**, 91 (1996).
- [8] J. Blomgren, B. Granbom, T. Granlund, and N. Olsson, Mat. Res. Soc. Bull. **28**, 121 (2003).
- [9] D. T. Bartlett, R. Grillmaeir, W. Heinrich, L. Lindborg, D. O'Sullivan, H. Schraube, M. Silari, L. Tommasino, Radiat. Res. Cong. Proc. **2**, 719 (2000).
- [10] R. W. Finlay, W. P. Abfalterer, G. Fink, E. Montei, T. Adami, P. W. Lisowski, G. L. Morgan, and R. C. Haight, Phys. Rev. C **47**, 237 (1993).
- [11] J. Rapaport and E. Sugarbaker, Annu. Rev. Nucl. Part. Sci. **44**, 109 (1994).
- [12] W. P. Alford and B. M. Spicer, Adv. Nucl. Phys. **24**, 1 (1998).
- [13] V. G. J. Stoks, R. A. M. Klomp, M. C. M. Rentmeester, and J. de Swart, Phys. Rev. C **48**, 792 (1993).
- [14] R. P. DeVito, S. M. Austin, W. Sterrenburg, and U. E. P. Berg, Phys. Rev. Lett. **47**, 628 (1981).
- [15] R. P. DeVito, S. M. Austin, U. E. P. Berg, R. De Leo, and W. A. Sterrenburg, Phys. Rev. C **28**, 2530 (1983).
- [16] F. P. Brady, T. D. Ford, G. A. Needham, J. L. Romero, C. M. Castaneda, and M. L. Webb, Nucl. Instrum. Methods Phys. Res. A **228**, 89 (1984).
- [17] E. L. Hjort, F. P. Brady, J. L. Romero, J. R. Drummond, D. S. Sorenson, J. H. Osborne, B. McEachern, and L. F. Hansen, Phys. Rev. C **50**, 275 (1994).
- [18] M. Ibaraki, M. Baba, T. Miura, Y. Nauchi, Y. Hirasawa, N. Hirakawa, H. Nakashima, S. Meigo, O. Iwamoto, and S. Tanaka, J. Nucl. Sci. Technol., Suppl. **1**, 683 (2000).
- [19] M. Baba, M. Ibaraki, T. Miura, T. Aoki, Y. Hirasawa, H. Nakashima, S. Meigo, and S. Tanaka, J. Nucl. Sci. Technol., Suppl. **2**, 204 (2002).
- [20] A. Bratenahl, S. Fernbach, R. H. Hildebrand, C. E. Leith, and B. J. Moyer, Phys. Rev. **77**, 597 (1950).
- [21] G. L. Salmon, Nucl. Phys. **21**, 15 (1960).
- [22] C. P. van Zyl, R. G. P. Voss, and R. Wilson, Philos. Mag. **1**, 1003 (1956).
- [23] R. S. Harding, Phys. Rev. **111**, 1164 (1958).
- [24] A. Ashmore, D. S. Mather, and S. K. Sen, Proc. Phys. Soc. A **71**, 552 (1958).
- [25] J. Klug, J. Blomgren, A. Ataç, B. Bergenwall, A. Hildebrand, C. Johansson, P. Mermod, L. Nilsson, S. Pomp, U. Tippawan, K. Elmgren, N. Olsson, O. Jonsson, A. V. Prokofiev, P.-U. Renberg, P. Nadel-Turonski, S. Dangtip, P. Phansuke, M. Österlund, C. Le Brun, J. F. Lecolley, F. R. Lecolley, M. Louvel, N. Marie-Noury, C. Schweitzer, Ph. Eudes, F. Haddad, C.

- Lebrun, A. J. Koning, E. Bauge, J. P. Delaroche, M. Girod, X. Ledoux, P. Romain, D. G. Madland, K. Amos, P. K. Deb, S. Karataglidis, R. Crespo, and A. M. Moro, *Phys. Rev. C* **67**, 031601(R) (2003).
- [26] J. Klug, J. Blomgren, A. Ataç, B. Bergenwall, S. Dangtip, K. Elmgren, C. Johansson, N. Olsson, S. Pomp, A. V. Prokofiev, J. Rahm, U. Tippawan, O. Jonsson, L. Nilsson, P.-U. Renberg, P. Nadel-Turonski, A. Ringbom, A. Oberstedt, F. Tovesson, V. Blideanu, C. Le Brun, J. F. Lecolley, F. R. Lecolley, M. Louvel, N. Marie, C. Schweitzer, C. Varignon, Ph. Eudes, F. Haddad, M. Kerveno, T. Kirchner, C. Lebrun, L. Stuttgé, I. Slypen, A. Smirnov, R. Michel, S. Neumann, and U. Herpers, *Nucl. Instrum. Methods Phys. Res. A* **489**, 282 (2002).
- [27] H. Condé, S. Hultqvist, N. Olsson, T. Rönnqvist, R. Zorro, J. Blomgren, G. Tibell, A. Håkansson, O. Jonsson, A. Lindholm, L. Nilsson, P.-U. Renberg, A. Brockstedt, P. Ekström, M. Österlund, F. P. Brady, and Z. Szefflinski, *Nucl. Instrum. Methods Phys. Res. A* **292**, 121 (1990).
- [28] A. N. Smirnov, V. P. Eismont, and A. V. Prokofiev, *Radiat. Meas.* **25**, 151 (1995).
- [29] S. Dangtip, A. Ataç, B. Bergenwall, J. Blomgren, K. Elmgren, C. Johansson, J. Klug, N. Olsson, G. Alm Carlsson, J. Söderberg, O. Jonsson, L. Nilsson, P.-U. Renberg, P. Nadel-Turonski, C. Le Brun, F. R. Lecolley, J. F. Lecolley, C. Varignon, Ph. Eudes, F. Haddad, M. Kerveno, T. Kirchner, and C. Lebrun, *Nucl. Instrum. Methods Phys. Res. A* **452**, 484 (2000).
- [30] A. J. Koning and J. P. Delaroche, *Nucl. Phys.* **A713**, 231 (2003).
- [31] S. Y. van der Werf (private communication).
- [32] R. Schaefer and J. Raynal, program DWBA70; J. R. Comfort, extended version DW81.
- [33] S. Cohen and D. Kurath, *Nucl. Phys.* **73**, 1 (1965).
- [34] B. A. Brown, A. Etchegoyen, and W. D. M. Rae, program OXBASH, MSUCL Report No. 524, 1988.
- [35] H. V. von Geramb, in *Interactions Between Medium Energy Nucleons in Nuclei*, edited by H. O. Meyer (AIP, New York, 1983), p. 44.
- [36] A. Nadasen, P. Schwandt, P. P. Singh, W. W. Jacobs, A. D. Bacher, P. T. Debevec, M. D. Kaitchuck, and J. T. Meek, *Phys. Rev. C* **23**, 1023 (1981).
- [37] K. Strauch and F. Titus, *Phys. Rev.* **103**, 200 (1956).
- [38] S. K. Mark, P. M. Portner, and R. B. Moore, *Can. J. Phys.* **44**, 2961 (1966).
- [39] J. Rahm, J. Blomgren, H. Condé, S. Dangtip, K. Elmgren, N. Olsson, T. Rönnqvist, R. Zorro, A. Ringbom, G. Tibell, O. Jonsson, L. Nilsson, P.-U. Renberg, T. E. O. Ericson, and B. Loiseau, *Phys. Rev. C* **57**, 1077 (1998).
- [40] R. C. Byrd and W. C. Sailor, *Nucl. Instrum. Methods Phys. Res. A* **264**, 494 (1989).
- [41] B. Holmqvist, B. Gustavsson, and T. Wiedling, *Ark. Fys.* **34**, 481 (1967).
- [42] J. DeJuren and N. Knable, *Phys. Rev.* **77**, 606 (1950).
- [43] R. G. P. Voss and R. Wilson, *Proc. R. Soc. London, Ser. A* **236**, 41 (1956).
- [44] R. W. Finlay (private communication).
- [45] P. F. Rose and C. L. Dunford, Technical Report No. BNL-NCS-44945 (Brookhaven National Laboratory, National Nuclear Data Center, Upton, NY, 1991); V. McLane, Technical Report No. BNL-NCS-17541 (4th ed. Suppl. 1) (Brookhaven National Laboratory, National Nuclear Data Center, Upton, NY, 1996). For internet access, see [www.nndc.bnl.gov](http://www.nndc.bnl.gov)
- [46] C. Johansson *et al.* (unpublished); J. Blomgren, spokesperson, TSL experiment FA 113 (unpublished).
- [47] R. Kozack and D. G. Madland, *Nucl. Phys.* **A509**, 664 (1990).
- [48] R. Kozack and D. G. Madland, *Phys. Rev. C* **39**, 1461 (1989).
- [49] B. D. Serot and J. D. Walecka, *Adv. Nucl. Phys.* **16**, 1 (1986).
- [50] P. Romain and J. P. Delaroche, in *Proceedings of a Specialists Meeting*, edited by P. Nagel (OECD, Paris, 1997), p. 167, see <http://db.nea.fr/html/science/om200/>
- [51] F. Perey and B. Buck, *Nucl. Phys.* **32**, 353 (1962).
- [52] K. Amos, P. J. Dortmans, H. V. von Geramb, S. Karataglidis, and J. Raynal, *Adv. Nucl. Phys.* **25**, 275 (2000).
- [53] R. Machleidt, *Adv. Nucl. Phys.* **19**, 189 (1989).
- [54] E. Bauge, J. P. Delaroche, and M. Girod, *Phys. Rev. C* **63**, 024607 (2001).
- [55] J. P. Jeukenne, A. Lejeune, and C. Mahaux, *Phys. Rev. C* **16**, 80 (1977).
- [56] R. Crespo, R. C. Johnson, and J. A. Tostevin, *Phys. Rev. C* **46**, 279 (1992).
- [57] G. Gerstein, J. Niederer, and K. Strauch, *Phys. Rev.* **108**, 427 (1957).
- [58] J. Matero, *Z. Phys. A* **351**, 29 (1995).
- [59] G. C. Wick, *Atti R. Accad. Naz. Lincei, Mem. Cl. Sci. Fis., Mat. Nat.* **13**, 1203 (1943).
- [60] G. C. Wick, *Phys. Rev.* **75**, 1459 (1949).
- [61] N. Olsson, B. Trostell, E. Ramström, B. Holmqvist, and F. S. Dietrich, *Nucl. Phys.* **A472**, 237 (1987).
- [62] J. H. Coon, R. W. Davis, H. E. Felthaus, and D. B. Nicode-mus, *Phys. Rev.* **111**, 250 (1958).
- [63] P. E. Hodgson, *The Optical Model of Elastic Scattering* (Oxford University Press, Oxford, 1963), p. 34.
- [64] ICRU Report No. 63 (International Commission on Radiation Units and Measurements, Bethesda, MD, 2000).
- [65] P. G. Young, E. D. Arthur, and M. B. Chadwick, Technical Report No. LA-12343-MS (Los Alamos National Laboratory, Los Alamos, NM, 1992).
- [66] J. Raynal, Technical Report No. CEA-N-2772 (Commisariat à l'Énergie Atomique, Saclay, France, 1994), pp. 1–145.
- [67] O. Bersillon, Technical Report No. CEA-N-2037 (Commisariat à l'Énergie Atomique, Saclay, France, 1978), pp. 111–120.
- [68] J. Rahm, J. Blomgren, H. Condé, S. Dangtip, K. Elmgren, N. Olsson, T. Rönnqvist, R. Zorro, O. Jonsson, L. Nilsson, P.-U. Renberg, A. Ringbom, G. Tibell, S. Y. van der Werf, T. E. O. Ericson, and B. Loiseau, *Phys. Rev. C* **63**, 044001 (2001).
- [69] P. Mermod *et al.* (unpublished); J. Blomgren, spokesperson, TSL experiment FA 148 (unpublished).
- [70] M. Österlund *et al.* (unpublished); J. Blomgren, spokesperson, TSL experiment FA 144 (unpublished).
- [71] A. Hildebrand *et al.* (unpublished); J. Blomgren, spokesperson, TSL experiment FA 144 (unpublished).
- [72] N. Olsson, H. Condé, E. Ramström, T. Rönnqvist, R. Zorro, J. Blomgren, A. Håkansson, G. Tibell, O. Jonsson, L. Nilsson, P.-U. Renberg, A. Brockstedt, P. Ekström, M. Österlund, S. Y. van der Werf, D. J. Millener, G. Szefflinska, and Z. Szefflinski, *Nucl. Phys.* **A559**, 368 (1993).